EES Solar

PAPER

View Article Online
View Journal

Cite this: DOI: 10.1039/d6el00027d

Hydrogen migration, surface accumulation, and nonradiative recombination in perovskite solar cells

Yong Huang,†[a] Xiqi Yang,†[a] Xiaoqing Chen,*[a] Rongkun Zhou,[a] He Huang,[a] Di Lu,[a] Yongcai He,[a] Wencai Zhou,*[b] Hui Yan[a] and Zilong Zheng *[a]

Perovskite solar cells (PSCs) have achieved efficiencies exceeding 27%, yet their performance remains limited by defect-induced nonradiative recombination. Although hydrogen interstitials (H_i) are conventionally considered as bulk defects, this study reveals the dynamic instability of H_i within the bulk lattice of $FAPbI_3$, which drives spontaneous migration to surface sites due to thermodynamic stabilization at the interface. By combining all-atom molecular dynamics (AAMD) with nonadiabatic molecular dynamics (NAMD), we elucidate the migration pathway of H_i and its electronic implications. Surface-trapped H_i induces significant lattice distortion, resulting in the formation of deep-level defect states and a modified potential energy landscape. This reorganization reduces the electron capture barrier (ΔE_n decreasing from 0.09 eV to 0.03 eV) and the hole capture barrier (ΔE_p dropping from 0.24 eV to 0.17 eV), and increases carrier capture coefficients by an order of magnitude (from 10^{-8} cm^3 s^{-1} to 10^{-7} cm^3 s^{-1}). Strengthened vibronic interactions and enhanced nonadiabatic couplings shorten the carrier lifetime from 0.8 ns (bulk H_i) to 0.1 ns (surface H_i), indicating surface-accumulated H_i is the dominant nonradiative recombination source rather than bulk H_i. These findings emphasize that interfacial hydrogen management, rather than conventional bulk passivation, is critical for designing suppression strategies to overcome performance limitations in PSCs.

Received 12th February 2026
Accepted 11th April 2026

DOI: 10.1039/d6el00027d

rsc.li/EESSolar

Broader context

Perovskite solar cells (PSCs) face fundamental efficiency limits from defect-induced recombination. While hydrogen interstitial (H_i) defects are recognized as detrimental, their dynamic behavior and spatial redistribution have been significantly overlooked. This work establishes that H_i in $FAPbI_3$ are intrinsically unstable in the bulk lattice and migrate spontaneously to surface sites, where they achieve thermodynamic stabilization. This surface accumulation induces severe lattice distortion and deep-level trapping state that enhance carrier capture coefficients and reduce carrier lifetimes by nearly an order of magnitude compared to bulk-located defects. Our findings shift the focus of defect management by demonstrating that interfacial hydrogen, rather than its bulk form, dominates recombination losses. This new understanding resolves a critical limitation of conventional bulk passivation, which proves inadequate for managing high-mobile defects. This conclusion is supported by recent advances in passivation strategies, for instance multifunctional molecules that simultaneously engage with surface defects and co-modification approaches that reconstruct the perovskite surface to suppress defect activity. By connecting hydrogen migration dynamics with interfacial recombination kinetics, this study provides an understanding of mobile defects in soft lattice materials. These insights are essential for overcoming efficiency limitations in PSCs and provide strategic guidance for defect engineering in related semiconductor technologies.

Introduction

Metal-halide perovskites have emerged as one of the most promising photovoltaic materials, due to their outstanding optoelectronic properties, facile solution processability, and rapid efficiency improvements.[1,2] Perovskite solar cells (PSCs) have achieved certified power conversion efficiencies (PCE) exceeding 27%,[3] positioning them as competitive contenders against established photovoltaic technologies. However, this remarkable progress remains constrained by the Shockley–Queisser (SQ) limit of 33%,[4] as defect-induced nonradiative recombination constitutes the dominant energy loss mechanism that limits device performance. The minimization of trap-assisted nonradiative recombination (or Shockley-Read-Hall, SRH) process has therefore become a critical direction for performance enhancement in PSCs.[5–7]

Extensive investigation over the past decade has explored the defect physics in metal halide perovskites through combined

[a]State Key Laboratory of Materials Low-Carbon Recycling, Beijing Key Lab of Microstructure and Properties of Advanced Materials, College of Materials Science and Engineering, School of Information Science and Technology Key Laboratory Optoelectronics Technology of Ministry of Education, Beijing University of Technology, Beijing 100124, China. E-mail: zilong.zheng@bjut.edu.cn; chenxiaoqing@bjut.edu.cn

[b]Hubei Key Lab of Photoelectric Materials and Devices, School of Materials Science and Engineering, Hubei Normal University, Huangshi, Hubei 435002, China. E-mail: zwc@hbnu.edu.cn

† Yong Huang, Xiqi Yang contributed equally to this paper.

experimental and theoretical approaches. Early research focused predominantly on B-site (Pb) and X-site (I) defects as principal nonradiative recombination centers, consistent with the orbital characteristics of the band edge states.[8] More studies have revealed the significant role of hydrogen-related defects originating from the A-site (MA and FA) cation deprotonation. For instance, hydrogen vacancies (V_H)[9] and hydrogen interstitials (H_i),[10] have been identified as major contributors to nonradiative losses in $MAPbI_3$ and $FAPbI_3$ perovskites.

In contrast to V_H, which exhibit self-healing behavior through coordination with lattice ions thereby suppressing their carrier capture coefficients,[11–13] H_i present a more severe challenge to device stability and performance. H_i form persistent deep-level traps that induce significant nonradiative recombination within the bulk lattice.[10] More critically, H_i exhibit high mobility with low migration potential barrier (0.17 eV) and strong thermodynamic driving force for redistribution.[14–16] This unfavorable combination may promote the dynamic accumulation of H_i at charge sensitive regions such as surfaces.[17] The H_i migration behavior has been experimentally confirmed and further accelerated under illumination and humidity,[18,19] providing a mechanistic explanation for observed device instabilities, including current–voltage hysteresis, surface recombination, and environmental degradation.

Conventional bulk passivation strategies, for instance halogen mixing and alkali-metal incorporation, have demonstrated restricted effectiveness in mitigating H_i defects due to their inherent high mobility.[20–23] This limitation becomes particularly significant when considering the distinct physical and chemical environment present in perovskite, where differences exist between bulk and surface regions that can fundamentally modify defect energetics and dynamics.[24] The variation in local coordination and chemical potential suggests that surface-accumulated H_i may exhibit different recombination characteristics compared to bulk-located H_i. This critical divergence between surface and bulk H_i behavior highlights a fundamental knowledge gap in understanding the microscopic mechanisms and recombination impact of surface-accumulated H_i defects.

To address this challenge, we employed a multiscale computational framework integrating density-functional theory (DFT), all-atom molecular dynamics (AAMD), and nonadiabatic molecular dynamics (NAMD) to investigate the H_i migration and carrier capture kinetics from bulk to surface in $FAPbI_3$. This approach combines the strengths of AAMD in capturing defect migration dynamics over nanosecond scales, the accuracy of DFT in determining electronic structures and defect energetics, and the capability of NAMD in simulating nonradiative carrier recombination processes. We find that H_i are intrinsically unstable in the bulk lattice, spontaneously migrating to surface sites within sub-nanosecond timescales due to a strong thermodynamic driving force, where they become energetically stabilized. This surface accumulation leads to a pronounced alteration in the defect electronic activity. The charge carrier capture barriers are significantly reduced, which in turn elevates the nonradiative carrier capture coefficient by an order of magnitude. Consequently, the carrier lifetime is drastically shortened from 0.8 ns for bulk-located H_i to 0.1 ns for surface-accumulated H_i, indicating surface-rich H_i as a severe recombination center that limits the performance of PSCs.

This work delivers fundamental insights into the surface-dominated H_i recombination. By connecting hydrogen migration dynamics with surface stabilization mechanisms and carrier capture kinetics, our findings highlight interfacial hydrogen management as an essential strategy for advancing high-performance PSCs.

Results and discussion

Migration dynamics and surface stabilization of H_i

In order to investigate the migration and stabilization behavior of H_i in $FAPbI_3$, we performed large-scale all-atom molecular dynamics (AAMD) simulations. This approach effectively addresses the constraints of both length and time scales in *ab initio* molecular dynamics (AIMD), enabling the tracking of H_i dynamics across microsecond-scale trajectories and over system sizes spanning hundreds of nanometers. The extended simulation capability allows for exploring H_i pathways and configurational relaxation toward thermodynamic minima.

The migration trajectory of H_i at 300 K is depicted in Fig. 1a. When initially positioned in the bulk region approximately 6 nm below the surface (Fig. 1b), H_i exhibits continuous directional drift toward the surface along with random thermal fluctuations, indicating a thermodynamic preference for surface accumulation. At the beginning (0–0.6 ns), H_i exhibited high mobility through rapid localized motion within neighboring unit cells. Subsequent migration to the surface (0.6–0.9 ns) is followed by lateral confinement and two-dimensional diffusion (0.9–1.2 ns), confirming surface stabilization.

The thermodynamic driving force for this behavior is clarified by the potential energy profile along the direction perpendicular to the surface, as shown in Fig. 1c. A pronounced energy minimum obtained at the surface region provides a quantitative explanation for the spontaneous accumulation of H_i, confirming that the surface possesses a lower energy state compared to the bulk. This potential energy gradient drives both directional migration and subsequent stabilization of H_i at the surface under room-temperature conditions.

Surface-induced modifications in H_i electronic structure

Based on the surface accumulation tendency of H_i in $FAPbI_3$, we further investigated how surface environments influence their local atomic arrangements and electronic properties. Comparative studies between bulk and surface configurations show that surface accumulation affects both H_i stability and electronic characteristics. In bulk regions, positive H_i^+ forms an H–I bond (1.75 Å), while neutral H_i^0 preferentially occupy the interstitial site between adjacent Pb–I bonds, forming a Pb–H–I bridging configuration. Additional electron capture generated H_i^-, resulting in noticeable PbI_6 octahedral distortion and stretching the opposing Pb–I bond to 4.22 Å (Fig. 2c). Surface environments introduce changes to these configurations, particularly for H_i^- which shows enhanced distortion that

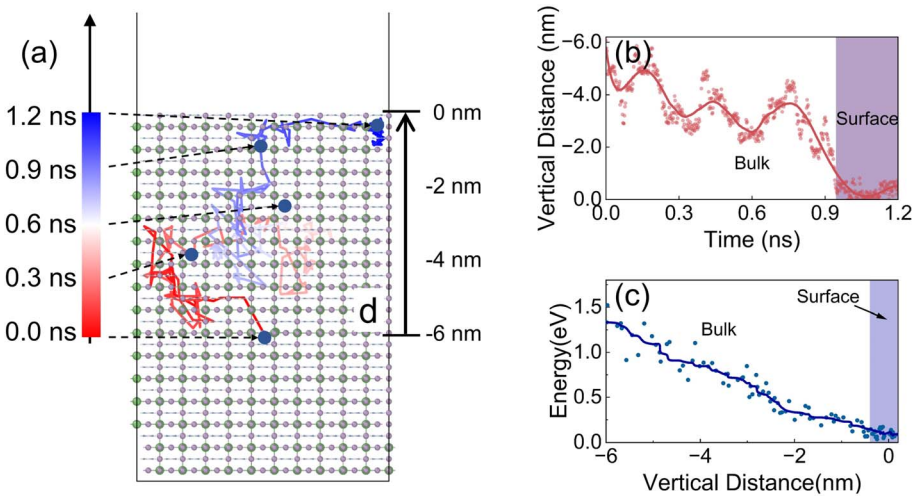

Fig. 1 (a) Migration trajectory showed H_i spontaneously moving from an initial depth of 6 nm in the bulk region to the surface within 0.9 ns, followed by trapping and lateral diffusion at the interface (0.9–1.2 ns). (b) Time evolution of H_i vertical distance from the surface, illustrating its rapid approach and subsequent stabilization at the interface. (c) Potential energy profile perpendicular to the surface, showing a distinct minimum at the interface that explains the thermodynamic preference for surface accumulation at 300 K.

breaks the Pb–I bond and extends it to 4.80 Å (Fig. 2d), indicating stronger electron-phonon interactions at the surface.

H_i formation energies and charge-state transition levels show modifications in surface environments, see Fig. 3. H_i introduces three distinct charge-state transition levels within the bandgap, $\varepsilon(\pm)$, $\varepsilon(0/-)$ and $\varepsilon(+/0)$. The $\varepsilon(\pm)$ transition involves a two-electrons capture process, which is less probable and therefore contributes weakly to nonradiative recombination. Consequently, the overall recombination kinetics are predominantly governed by the single-carrier capture transitions $\varepsilon(0/-)$ and $\varepsilon(+/0)$.[25] In the bulk, the $\varepsilon(0/-)$ level sits 0.41 eV above the valence band maximum (VBM), while $\varepsilon(+/0)$ lies 0.32 eV below the conduction band minimum (CBM), indicating the role of H_i as a recombination center. Surface accumulation shifts these levels to 0.53 eV above VBM and 0.38 eV below CBM, with $\varepsilon(0/-)$ moving 0.12 eV closer to the conduction band, consistent with the enhanced lattice relaxation seen in surface-stabilized H_i in Fig. 2.

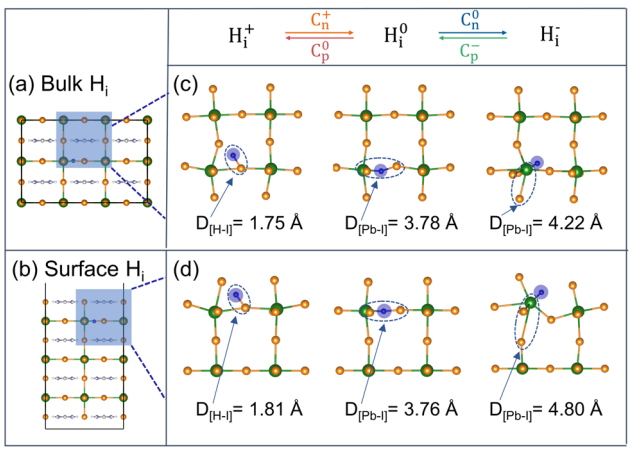

Fig. 2 (a and b) Computational models for H_i in bulk and surface slab. (c and d) Equilibrium configuration of H_i in charge states +, 0 and − in bulk and at surface, respectively. In the bulk, H_i^+ forms H–I bond, H_i^0 adopts a bond-center configuration, and H_i^- forms distorted H–Pb coordination with octahedral deformation. Electron capture transitions (C_n^+ and C_n^0) and hole capture transitions (C_p^- and C_p^0) corresponding to charge-state changes were indicated.

Enhanced carrier capture kinetics at surface sites

While Shockley-Read-Hall theory indicates carrier capture rates decline exponentially with the deeper transition levels, this relationship requires examination through potential energy surface (PES) calculations. We employed a one-dimensional quantum model to map PES for charge-state transitions along the configuration coordinate (Q),[26] defined through mass-weighted atomic displacements between initial and final configurations. This approach provides quantitative energies of carrier capture barrier.

$$\Delta Q^2 = \sum_{\alpha} m_{\alpha} \left(R_{\alpha;\mathrm{f}} - R_{\alpha;\mathrm{i}}\right)^2$$

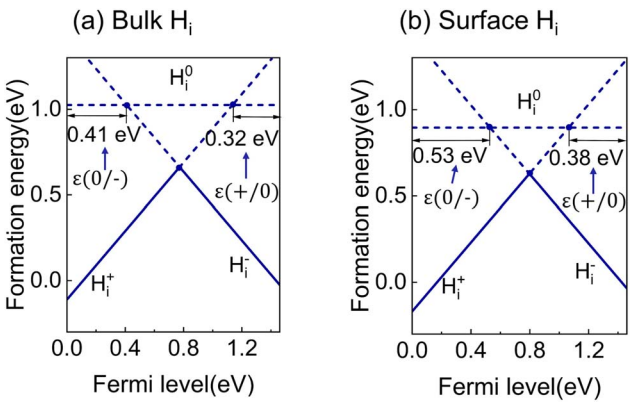

Fig. 3 Formation energies of H_i as a function of Fermi level under H-rich conditions for (a) bulk and (b) surface configurations, respectively.

where ΔQ is the displacement of Q coordinate; m_α is the mass of atom α in the configurations of defects; $R_{\alpha;f}$ and $R_{\alpha;i}$ are the Cartesian coordinates of atom α in the final and initial defect configurations.

The neutral H_i^0 introduces deep-level defect states within the bandgap, in contrast to the shallow states associated with H_i^+ and H_i^- defects, as discussed later. The configuration coordinate diagram showes carrier capture processes. For the $H_i^+ \leftrightarrow H_i^0$ transition, following photoexcitation, the system progresses through three distinct stages. Initially, H_i^+ remains inactive toward carrier capture, denoted as $H_i^+\cdots e^-\cdots h^+$; subsequently, electron capture transitions the defect to H_i^0, denoted as $(H_i^+ + e^-)\cdots h^+$; finally, hole capture returns the system to H_i^+, denoted as $(H_i^+ + e^- + h^+)$, see Fig. 4a. The capture potential barriers were obtained from the saddle point on the PES. The electron capture barrier ΔE_n^+) corresponds to the energy at saddle point between $H_i^+\cdots e^-\cdots h^+$ and $(H_i^+ + e^-)\cdots h^+$ transition; while hole capture barrier (ΔE_p^0) is derived from saddle point between $(H_i^+ + e^-)\cdots h^+$ and $(H_i^+ + e^- + h^+)$ transition.

For the (+/0) transition of bulk H_i, the associated configuration-coordinate displacement is $\Delta Q = 14.4$ Å amu$^{1/2}$. The corresponding electron capture process falls within the Marcus inverted region, characterized with a relative small configuration coordinate $Q = 2.6$ Å amu$^{1/2}$ ($0 < Q < \Delta Q$). In this regime, the ΔE_n^+ decreases as the (0/+) level shifts deeper below the CBM. In contrast, hole capture occurs in the Marcus normal region with $Q = 16.4$ Å amu$^{1/2}$ ($Q > \Delta Q$), resulting in an increased ΔE_p^0 with rising transition energy relative to the VBM. With the (+/0) level located at 0.32 eV below the CBM, the resulting energy barriers are $\Delta E_n^+ = 0.13$ eV for electron capture and small $\Delta E_p^0 = 0.08$ eV for hole capture. These values yield carrier capture coefficients of 2.0×10^{-8} cm^3 s^{-1} for electrons (C_n^+) and 2.8×10^{-7} cm^3 s^{-1} for holes (C_p^0) at room temperature, see Fig. 4c. The modest barriers and efficient capture processes confirm H_i as an effective nonradiative recombination center in bulk regions.

The (0/−) transition of bulk H_i, exhibits distinct characteristics due to large lattice relaxation ($\Delta Q = 31.9$ Åamu$^{1/2}$), with both electron and hole capture processes occurring in the Marcus inverted regions ($0 < Q < \Delta Q$). The (0/−) transition level are positioned at 0.41 eV above the VBM. The smaller electron capture barrier ($\Delta E_n^0 = 0.09$ eV) compared to hole capture barrier ($\Delta E_p^- = 0.24$ eV) results in a significantly disparity in capture coefficients. The electron capture coefficient (C_n^0) reached 1.2×10^{-6} cm^3 s^{-1}, whereas the hole capture coefficient (C_p^-) is limited to 1.9×10^{-8} cm^3 s^{-1}. Therefore, the overall capture coefficient (C_{tot}) is governed by the slower hole capture process, with the value of 1.9×10^{-8} cm^3 s^{-1}, derived from following equations under steady-state conditions.[27]

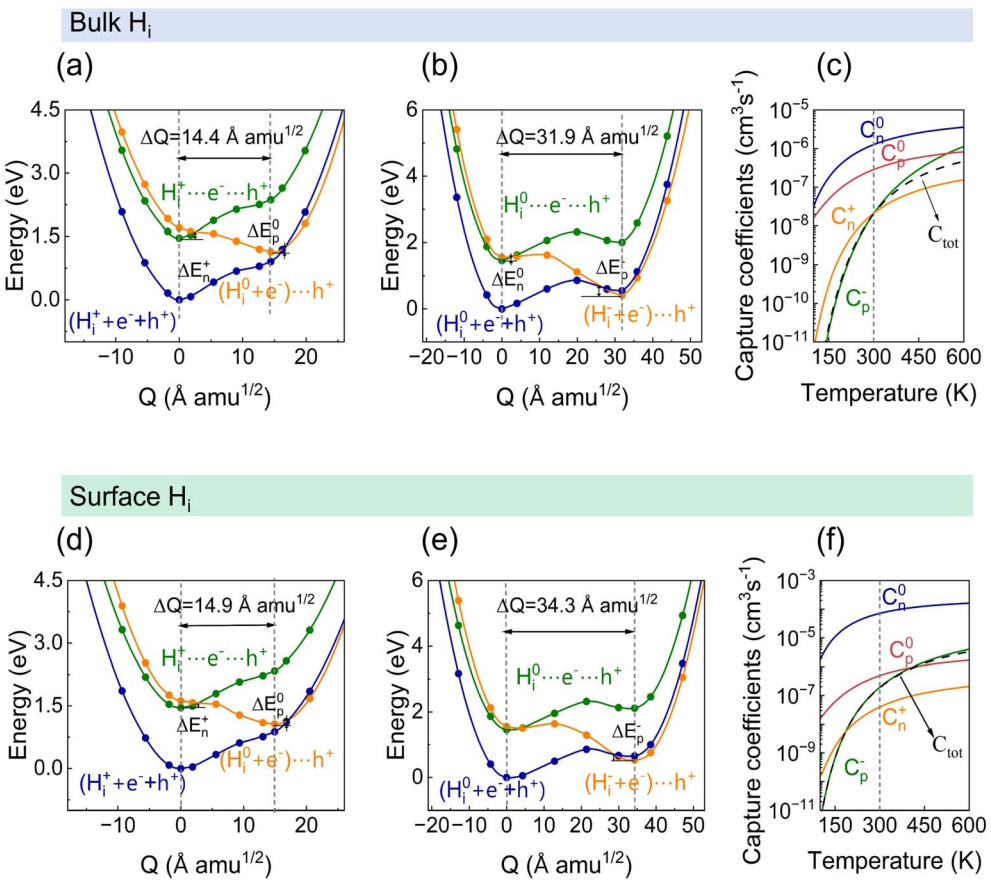

Fig. 4 (a and b) Configuration coordinate diagrams of (+/0) and (0/−) charge state transitions of bulk H_i in $FAPbI_3$. (c) Carrier capture coefficients as a function of temperature for bulk H_i. (d and e) Configuration coordinate diagrams of (+/0) and (0/−) charge state transitions of surface H_i. (f) Carrier capture coefficients as a function of temperature for surface H_i.

$$C_{tot} = \frac{C_n^{\,0} + C_p^{\,0}}{1 + \frac{C_n^{\,0}}{C_p^{-}} + \frac{C_p^{\,0}}{C_n^{+}}}$$

H_i surface-trapping substantially modifies these capture kinetics. Surface H_i exhibit larger lattice relaxation $\Delta Q = 34.3$ Å amu$^{1/2}$ (see Fig. 4d and e), yielding softer PESs and lower capture barriers for both electrons and holes. For the (0/−) transtion level, the electron capture barrier (ΔE_n^0) decreases from 0.09 eV (bulk H_i) to 0.03 eV (surface H_i), while the hole capture barrier (ΔE_p^-) drops from 0.24 eV (bulk H_i) to 0.17 eV (surface H_i). These reduced energy barriers lead to a rise in both C_n^0 (up to 7.0×10^{-5} cm^3 s^{-1}) and C_p^- (up to 1.8×10^{-7} cm^3 s^{-1}) by over one order of magnitude, see Fig. 4f. The overall C_{tot} remained limited by the slower hole capture process of H_i^-, yielding $C_{tot} = 1.8 \times 10^{-7}$ cm^3 s^{-1} at 300 K, approximately an order of magnitude higher than that in bulk (1.9×10^{-8} cm^3 s^{-1}).

Nonadiabatic dynamics of H_i recombination

To elucidate the real-time carrier recombination dynamics mediated by H_i, we performed nonadiabatic molecular dynamics (NAMD) simulations. This approach couples electronic transitions with atomic motions, capturing the ultrafast timescales and mechanisms of defect-assisted nonradiative recombination that extend beyond static multi-phonon emission models.[28,29]

Our electronic structure results revealed that among three charged states of H_i (H_i^+, H_i^0, H_i^-), only the neutral H_i^0 introduces a persistent deep-level defect state within the bandgap. While H_i^+ has a negligible influence on the band edges, and H_i^- forms only shallow defect states level 0.16 eV away from the band edge (Fig. S1 and S2 in SI), H_i^0 creates a localized state that acts as a recombination center. Notably, this defect level deepens from being 0.53 eV away from the band edge in the bulk to 0.84 eV at the surface. Therefore, H_i^0 was considered as the dominant recombination active species and all subsequent NAMD analysis focused on its behavior. The charge densities of the defect states for both bulk H_i and surface H_i were provided in Fig. S3 of SI.

To explore the phonon-driven recombination mechanism, we calculated the spectral density *via* Fourier transform of the fluctuations in the energy gaps between relevant states, including CBM-VBM, CBM-Trap, VBM-Trap (see Fig. 5b and e). Each peak in the spectral density characterizes the strength of electron-phonon coupling for a specific phonon mode. The results indicated that the CBM-VBM energy gap coupling is dominated by low-frequency phonon modes (below 100 cm^{-1}), which are associated with Pb–I lattice bending and stretching.[30,31] In contrast, the energy gaps involving the H_i^0 trap state (CBM-Trap and VBM-Trap) are significantly modulated by

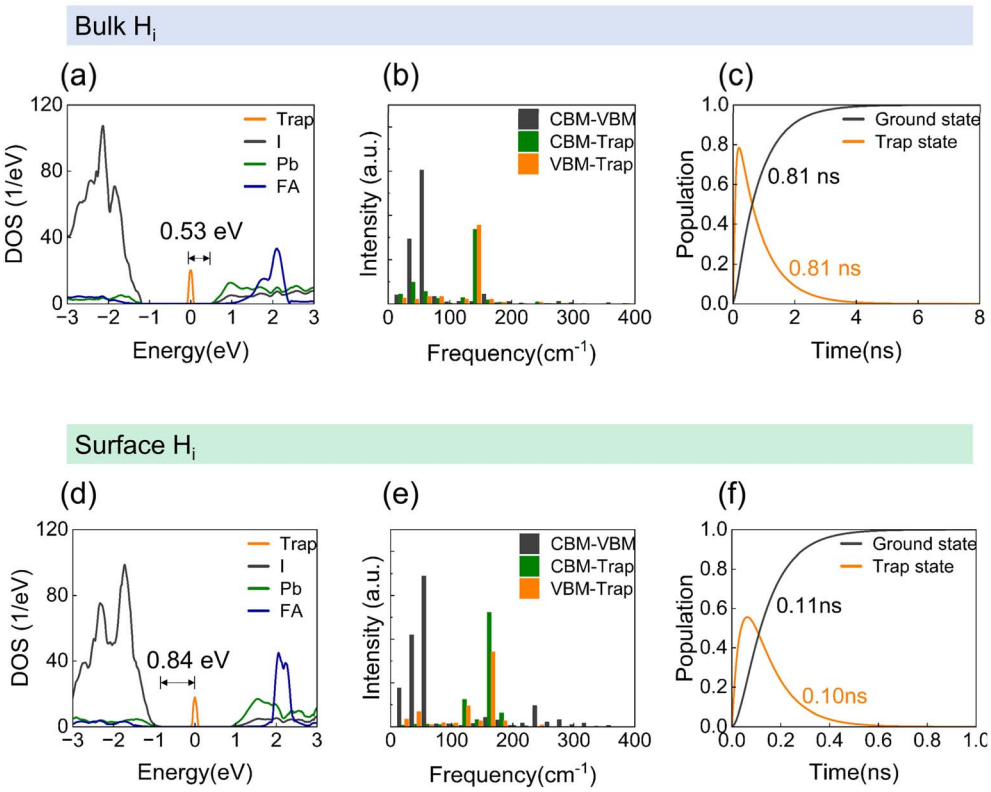

Fig. 5 (a) Projected density of states (PDOS) of bulk H_i. (b) Spectra density for bulk H_i, obtained from Fourier transform of the auto-correlation functions for the CBM-VBM, CBM-trap, and VBM-trap transitions. (c) Nonradiative electron–hole recombination dynamics for bulk H_i. (d) PDOS of surface H_i. (e) Spectra density for surface H_i obtained from Fourier transform of the auto-correlation functions for CBM-VBM, CBM-trap, VBM-trap transitions. (f) Nonradiative electron–hole recombination dynamics for surface H_i.

higher-frequency modes (100–300 cm^{-1}) originating from the vibrations and torsions of organic FA molecules.[30] This suggests that organic cation dynamics play an indirect but crucial role in the nonradiative recombination process mediated by H_i^0.

Although H_i^0 defect couples to similar phonon modes in both bulk and surface environments, the coupling intensity is stronger at the surface. This enhancement arises from under-coordinated surface iodide ions and increased rotational freedom of FA cations near the surface. These stronger vibronic interactions also accelerated electronic decoherence, as confirmed by the dephasing functions obtained from the second-order cumulant expansion of the energy gaps correlation functions (see Fig. S4 in SI).[32,33] Our calculated decoherence times for the bulk are 9.9 fs (CBM-VBM), 3.5 fs (CBM-Trap), and 3.8 fs (VBM-Trap), consistent with previous reports.[34–36] Surface H_i^0 exhibited even shorter decoherence times of 4.7 fs (CBM-VBM), 2.3 fs (CBM-Trap), and 2.4 fs (VBM-Trap), reflecting the stronger dynamic disorder at the surface. Although faster decoherence can, in principle, slow down the recombination rates, our findings indicated recombination is significantly accelerated at the surface. This implies that decoherence is not the rate-limiting factor here, prompting the following investigation into the non-adiabatic couplings (NAC).

We therefore quantified the NAC strength, $\varphi_i|\nabla_R|\varphi_f$, which governs the probability of electronic transitions and is correlated with the wavefunction overlap between initial (φ_i) and final (φ_f) states. The results were summarized in Table 1 and S1. In the bulk, the CBM-to-VBM NAC was negligible (0.3 meV), leading to a very slow band-to-band recombination rate (0.008 ns^{-1}). In contrast, NAC value between the H_i^0 trap state and the band edges was substantially larger (2.5 meV for CBM-Trap and 0.8 meV for VBM-Trap), resulting in much faster defect-assisted trapping rates of 15.8 ns^{-1} (electron capture) and 1.2 ns^{-1} (hole capture).

Critically, at the surface, the defect-mediated NACs increased to 1.9 meV (CBM-trap) and 2.9 meV (VBM-trap), while CBM-VBM coupling remained weak (0.2 meV). This enhancement, driven by the increased lattice distortion and wavefunction localization at the surface, resulted in electron and hole capture rates of 9.4 ns^{-1} and 25.4 ns^{-1}, respectively. Since the slower carryier capture process dictates the overall recombination rate, the surface recombination rate (9.4 ns^{-1}) is nearly an order of magnitude faster than that (1.2 ns^{-1}) in the bulk. These results indicated that H_i-induced severe nonradiative recombination at the surface is dominated by enhanced non-adiabatic coupling rather than quantum decoherence effects.

Finally, by integrating the effects of lattice vibration, quantum decoherence, and non-adiabatic coupling effects, we performed NAMD simulations to track the recombination kinetics, see Fig. 5c and f. For bulk H_i, approximately 80% of electrons in the CBM were captured by the trap state within tens of picoseconds, followed by recombination with holes in the VBM yielding an overall carrier lifetime of 0.8 ns. In contrast, for surface-accumulated H_i, an ultrafast hole capture process was followed by rapid recombination with CBM electrons, drastically shortening the carrier lifetime to 0.1 ns. This order-of-magnitude acceleration in recombination at the surface confirms that surface H_i acts as a detrimental nonradiative recombination center.

Table 1 Non-adiabatic (NA) couplings, dephasing times, and trapping rates for bulk H_i and surface H_i

		NA coupling (meV)	Dephasing (fs)	Rate (ns^{-1})
Bulk H_i	CBM-trap	2.5	3.5	15.8
	VBM-trap	0.8	3.8	1.2
Surface H_i	CBM-trap	1.9	2.3	9.4
	VBM-trap	2.9	2.4	25.4

Conclusion

In summary, this work reveals that hydrogen interstitials (H_i) in $FAPbI_3$ perovskite solar cells (PSCs) exhibit intrinsic dynamic instability within the bulk lattice, driving spontaneous migration to surface sites, where they achieve thermodynamic stabilization. The surface-accumulated H_i undergoes significant lattice reorganization, forming deep-level defect states that substantially enhance nonradiative recombination. Compared to bulk-positioned H_i, surface-accumulated H_i exhibits reduced electron capture barrier (ΔE_n from 0.09 eV to 0.03 eV) and hole capture barrier (ΔE_p from 0.24 eV to 0.17 eV), alongside an order of magnitude increase in carrier capture coefficients (from 10^{-8} cm^3 s^{-1} to 10^{-7} cm^3 s^{-1}). This leads to a drastic reduction in carrier lifetime from 0.8 ns to 0.1 ns. The accelerated recombination kinetics at the surface are primarily driven by strengthened vibronic interactions and strong nonadiabatic couplings. These findings establish surface-accumulated H_i, rather than conventional bulk H_i, as the dominant nonradiative recombination center in PSCs. This work underscores the importance of interfacial hydrogen management for suppressing nonradiative losses and provides a fundamental basis for designing advanced passivation strategies to overcome efficiency limitations in PSCs.

Conflicts of interest

There are no conflicts to declare.

Data availability

The data supporting this article have been included as part of the supplementary information (SI). Supplementary information: detailed computational methods, figures, kinetic equations, and table. See DOI: https://doi.org/10.1039/d6el00027d.

Acknowledgements

This work was financially supported by Beijing Natural Science Foundation (BNSF, Grants JQ23020), and Natural Science Foundation of China (NSFC, Grants 62034001, 62474013, and 22033006).

References

1 H. Wang, Y. Ge, W. Shao, X. Xiong, G. Li, N. Li, X. Hu, G. Chen, K. Dong, W. Ai, Z. Yu, Z. Zheng, C. Wang, F. Yao,

X. Cao, S. Li, J. Zhao, W. Ke, C. Tao, Y. Hou, A. Petrozza and G. Fang, Yttrium oxide engineered substrate enables improved durability for perovskite solar cells, *Nat. Commun.*, 2025, **16**, 9508.

2 Y. Liang, G. Chen, Y. Wang, Y. Zou, M. Feng, Y. Wang, B. Li, Y. Cho, Y. Chang, T. Liu, T. Zhang, Y. Lou, R. Xu, L. Lu, N. Zhang, K. Meng, C. Zhu, C. Ouyang, Y. Miao, Y. Guo, Y. Chen and Y. Zhao, A matrix-confined molecular layer for perovskite photovoltaic modules, *Nature*, 2025, **648**, 91–96.

3 Y. Yang, H. Chen, C. Liu, J. Xu, C. Huang, C. D. Malliakas, H. Wan, A. S. R. Bati, Z. Wang, R. P. Reynolds, I. W. Gilley, S. Kitade, T. E. Wiggins, S. Zeiske, S. Suragtkhuu, M. Batmunkh, L. X. Chen, B. Chen, M. G. Kanatzidis and E. H. Sargent, Amidination of ligands for chemical and field-effect passivation stabilizes perovskite solar cells, *Science*, 2024, **386**, 898–902.

4 W. Shockley and H. J. Queisser, Detailed balance limit of efficiency of p–n junction solar cells, *J. Appl. Phys.*, 1961, **32**, 510–519.

5 W.-J. Yin, T. Shi and Y. Yan, Unusual defect physics in ch3nh3pbi3 perovskite solar cell absorber, *Appl. Phys. Lett.*, 2014, 104.

6 D. J. Keeble, J. Wiktor, S. K. Pathak, L. J. Phillips, M. Dickmann, K. Durose, H. J. Snaith and W. Egger, Identification of lead vacancy defects in lead halide perovskites, *Nat. Commun.*, 2021, **12**, 5566.

7 W. Jia, R. Sun, J. Qiao, G. Shi, Q. Zhao, Z. Gong, S. Zheng, R. Xu, J. Shang, L. Song, K. Wang, W. Huang, R. Chen, Y. Fang, H. Wang and Z.-Q. Rong, Molecular design-driven interface engineering enabling simultaneous defect passivation and enhanced hole extraction in perovskite solar cells, *Angew. Chem., Int. Ed.*, 2025, **137**, e202513869.

8 N. Xu, X. Qi, Z. Shen, L. Hu, J. Lv, Y. Zhong, B. Wang and Z. Zou, Point defects in metal halide perovskites, *Nat. Rev. Phys.*, 2025, **7**, 554–564.

9 X. Zhang, J.-X. Shen, M. E. Turiansky and C. G. Van de Walle, Minimizing hydrogen vacancies to enable highly efficient hybrid perovskites, *Nat. Mater.*, 2021, **20**, 971–976.

10 Y. Liang, X. Cui, F. Li, C. Stampfl, S. P. Ringer, J. Huang and R. Zheng, Minimizing and controlling hydrogen for highly efficient formamidinium lead triiodide solar cells, *J. Am. Chem. Soc.*, 2022, **144**, 6770–6778.

11 W. Zhou, R. Zhou, X. Chen, Z. Zhou, Y. He, C. Qian, H. Yan, Z. Zheng, Y. Zhang and H. Yan, Synergy between dynamic behavior of hydrogen defects and non-radiative recombination in metal-halide perovskites, *Small*, 2024, **20**, 2405201.

12 W. Zhou, X. Yang, R. Zhou, H. Huang, Y. He, X. Chen, C. Qian, Z. Zheng and H. Yan, Impact of hydrogen vacancies on non-radiative recombination in metal-halide perovskites, *Angew. Chem.*, 2025, **137**, e202503394.

13 X. Tian, A. S. Vasenko, E. V. Chulkov and R. Long, Anharmonic motion-induced self-passivation of hydrogen defects in hybrid organic–inorganic perovskites: Ab initio quantum dynamics, *J. Phys. Chem. Lett.*, 2025, **16**, 10466–10472.

14 D. A. Egger, L. Kronik and A. M. Rappe, Theory of hydrogen migration in organic-inorganic halide perovskites, *Angew. Chem., Int. Ed.*, 2015, **54**, 12437–12441.

15 Y.-F. Chen, Y.-T. Tsai, L. Hirsch and D. M. Bassani, Kinetic isotope effects provide experimental evidence for proton tunneling in methylammonium lead triiodide perovskites, *J. Am. Chem. Soc.*, 2017, **139**, 16359–16364.

16 Y. Feng, Y. Zhao, W.-K. Zhou, Q. Li, W. A. Saidi, Q. Zhao and X.-Z. Li, Proton migration in hybrid lead iodide perovskites: From classical hopping to deep quantum tunneling, *J. Phys. Chem. Lett.*, 2018, **9**, 6536–6543.

17 M. Li, D.-G. Xie, E. Ma, J. Li, X.-X. Zhang and Z.-W. Shan, Effect of hydrogen on the integrity of aluminium-oxide interface at elevated temperatures, *Nat. Commun.*, 2017, **8**, 14564.

18 D. R. Ceratti, A. Zohar, R. Kozlov, H. Dong, G. Uraltsev, O. Girshevitz, I. Pinkas, L. Avram, G. Hodes and D. Cahen, Eppur si muove: Proton diffusion in halide perovskite single crystals, *Adv. Mater.*, 2020, **32**, 2002467.

19 S. Sadhu, T. Buffeteau, S. Sandrez, L. Hirsch and D. M. Bassani, Observing the migration of hydrogen species in hybrid perovskite materials through d/h isotope exchange, *J. Am. Chem. Soc.*, 2020, **142**, 10431–10437.

20 Y. Liang, X. Cui, F. Li, C. Stampfl, J. Huang, S. P. Ringer and R. Zheng, Hydrogen-anion-induced carrier recombination in mapbi3 perovskite solar cells, *J. Phys. Chem. Lett.*, 2021, **12**, 10677–10683.

21 X. Ma, Z. Liu, W.-H. Fang, R. Long and O. V. Prezhdo, Passivation of hydrogen interstitials in metal halide perovskites: A time-domain ab initio study, *J. Am. Chem. Soc.*, 2025, **147**, 25960–25968.

22 W. Cai, Y. Wang, W. Shang, J. Liu, M. Wang, Q. Dong, Y. Han, W. Li, H. Ma and P. Wang, Lewis base governing superfacial proton behavior of hybrid perovskite: Basicity dependent passivation strategy, *Chem. Eng. J.*, 2022, **446**, 137033.

23 P. Zhang, E. Stippell, Y. Chen, X. Du, Z. Hou, O. V. Prezhdo and W. Li, Atomistic mechanism of defect self-passivation in metal halide perovskites, *Nano Lett.*, 2025, **25**, 14140–14146.

24 J. Wang and W.-J. Yin, Revisiting the iodine vacancy surface defects to rationalize passivation strategies in perovskite solar cells, *J. Phys. Chem. Lett.*, 2022, **13**, 6694–6700.

25 N. T. Bagraev and V. A. Mashkov, A mechanism for two-electron capture at deep level defects in semiconductors, *Solid State Commun.*, 1988, **65**, 1111–1117.

26 A. Alkauskas, Q. Yan and C. G. Van de Walle, First-principles theory of nonradiative carrier capture via multiphonon emission, *Phys. Rev. B Condens. Matter*, 2014, **90**, 075202.

27 A. Alkauskas, C. E. Dreyer, J. L. Lyons and C. G. Van de Walle, Role of excited states in shockley-read-hall recombination in wide-band-gap semiconductors, *Phys. Rev. B*, 2016, **93**, 201304.

28 M. E. Turiansky, A. Alkauskas, M. Engel, G. Kresse, D. Wickramaratne, J.-X. Shen, C. E. Dreyer and C. G. Van de Walle, Nonrad: Computing nonradiative capture coefficients from first principles, *Comput. Phys. Commun.*, 2021, **267**, 108056.

29 A. Alkauskas, Q. Yan and C. G. Van de Walle, First-principles theory of nonradiative carrier capture via multiphonon emission, *Phys. Rev. B*, 2014, **90**, 075202.
30 C. Quarti, G. Grancini, E. Mosconi, P. Bruno, J. M. Ball, M. M. Lee, H. J. Snaith, A. Petrozza and F. De Angelis, The raman spectrum of the ch3nh3pbi3 hybrid perovskite: Interplay of theory and experiment, *J. Phys. Chem. Lett.*, 2013, **5**, 279–284.
31 A. M. A. Leguy, A. R. Goñi, J. M. Frost, J. Skelton, F. Brivio, X. Rodríguez-Martínez, O. J. Weber, A. Pallipurath, M. I. Alonso and M. Campoy-Quiles, Dynamic disorder, phonon lifetimes, and the assignment of modes to the vibrational spectra of methylammonium lead halide perovskites, *Phys. Chem. Chem. Phys.*, 2016, **18**, 27051–27066.
32 S. Mukamel, *Principles of Nonlinear Optical Spectroscopy*, New York: Oxford university press, 1995, 6, 543.
33 J. Liu, S. V. Kilina, S. Tretiak and O. V. Prezhdo, Ligands slow down pure-dephasing in semiconductor quantum dots, *ACS Nano*, 2015, **9**, 9106–9116.
34 G. Alkhalifah, B. Wang, O. V. Prezhdo and W.-L. Chan, Suppressing polaronic defect–photocarrier interaction in halide perovskites by pre-distorting its lattice, *J. Am. Chem. Soc.*, 2025, **147**, 2411–2420.
35 X. Ma, X. Tian, E. Stippell, O. V. Prezhdo, R. Long and W.-H. Fang, Self-passivation of halide interstitial defects by organic cations in hybrid lead-halide perovskites: Ab initio quantum dynamics, *J. Am. Chem. Soc.*, 2024, **146**, 29255–29265.
36 Z. Zhou, Y. Wu, J. He, T. Frauenheim and O. V. Prezhdo, Enhancing extraction and suppressing cooling of hot electrons in lead halide perovskites by dipolar surface passivation, *J. Am. Chem. Soc.*, 2024, **146**, 29905–29912.